

Realistic Multidimensional Optoelectrical Modeling Guide for Copper Indium Gallium Diselenide Solar Cells

Jan Lucaßen, Setareh Sedaghat, and Martina Schmid*

Herein, an optoelectrical model is presented for copper indium gallium diselenide (CIGSe) solar cells in COMSOL Multiphysics, capable of multidimensional simulations, and it is applied to ultrathin (500 nm absorber thickness) solar cells. First, the modeling approach is shown. Special attention is paid to back contact materials, interface states, and defect application and their impact on the current–voltage (J – V) characteristics. To address whether the back contact is Schottky or Ohmic, the influence of the Schottky barrier height, recombination velocity, and interface states is shown. Then, the additional application of an acceptor defect gradient at the absorber back and a donor defect density distribution at the p – n junction is investigated. The results of these parameter adjustments are discussed, and the trends are shown to enable fast fitting of experimental J – V curves. Finally, the results are compared to the experimental J – V curves for indium tin oxide and Mo back contact, and challenges encountered are discussed while fitting. The optoelectrical model for CIGSe solar cells, established in two dimensions here, paves the way for comprehensively describing 2D and 3D solar cell structures, e.g., nanotextured or microsolar cells, as well as for considering different absorber thicknesses.

lowering the absorber thickness from 2 microns to 0.5 microns shows great potential. It reduces the material consumption by 75% compared to a thick absorber. The record efficiency of an ultrathin (≤ 500 nm absorber thickness) CIGSe solar cell is 15.2%.^[2] Semitransparency is another technique for widening the field of application and increasing efficiency. For this purpose, the standard molybdenum back contact can be replaced with indium tin oxide (ITO). For further optimization of the ultrathin solar cells and to offer insight into the underlying physics, simulations yield a valuable and cost-effective tool. 1D simulations are sufficient for optical and electrical modeling of planar cells using platforms like SCAPS,^[3] but 2D and 3D models are indispensable if nanostructures, point contacts, or different geometries (e.g., microabsorber islands) are of interest.^[4–6] COMSOL Multiphysics enables multidimensional optical, electrical, and thermal simulations based on


1. Introduction

With a growing demand for solar energy, cost and sustainability play a significant role in research and industry. Chalcopyrites, like copper indium gallium diselenide (CIGSe), with their tunable bandgap and high absorption coefficient, are one of the promising thin-film technologies. They are suitable for many applications, such as car roofs, windows, and facades, because they are lightweight and can be semitransparent. However, the scarcity of indium and gallium influences the production costs for CIGSe absorbers.^[1] To save material, speed up the production process, and reduce CAPEX costs, the opportunity of

the finite element method (FEM). It was used here to develop a base parameter set capable of modeling ultrathin CIGSe solar cells on Mo or ITO back contact. There are multiple research works showing numerical simulation on the effect of layer thickness,^[7] the rear surface passivation mechanism,^[4] Al_2O_3 -rear-passivated,^[8] and interdigitated back contacted absorbers.^[5] Recently, an updated baseline model for 1D modeling of thin film and ultrathin absorbers in SCAPS has been proposed.^[9] All of the named publications used a Mo back contact. We intended to investigate the difference between Mo and ITO back contact and find out the reason for the similar behavior in the experimental results. Moreover, the parameter sets of the simulations differ slightly from each other. Therefore, we show the effect of different material parameters on the multidimensional simulation and how to adjust the simulation parameters to fit experimental results. We demonstrate the development of the model in 2D here for the sake of computational resources and the capability of cross-checking with realistic material properties on a planar reference structure. The implementation in more than 1D is, however, the base for a straightforward translation of the model to 3D, where all possible textures can be addressed.

According to the literature, the back contact barrier plays a pivotal role in optimizing the performance of CIGSe solar cells. The contacts of Mo/ITO with CIGSe should be considered Schottky-like contacts due to the metal/metal-like semiconductor junction. Despite numerous experimental works, it is unclear

J. Lucaßen, S. Sedaghat, M. Schmid
Faculty of Physics & CENIDE
University of Duisburg-Essen
47057 Duisburg, Germany
E-mail: martina.schmid@uni-due.de

 The ORCID identification number(s) for the author(s) of this article can be found under <https://doi.org/10.1002/solr.202200867>.

© 2022 The Authors. Solar RRL published by Wiley-VCH GmbH. This is an open access article under the terms of the Creative Commons Attribution-NonCommercial-NoDerivs License, which permits use and distribution in any medium, provided the original work is properly cited, the use is non-commercial and no modifications or adaptations are made.

DOI: 10.1002/solr.202200867

whether the back contact behavior is Ohmic, quasi-Ohmic, or Schottky, resulting from different fabrication techniques.^[10–13] For instance, the formation of MoSe₂ has been correlated to the Ohmic contact behavior of the Mo/CIGSe interface.^[11,14,15] The formation of the MoSe₂ layer is not the exclusively determining part of the Ohmic behavior, but also sodium doping and the MoSe₂ orientation play crucial roles in forming an Ohmic contact.^[16–18] For the CIGSe/ITO interface, the formation of a GaO_x layer has been proven. Nevertheless, there is a contradiction about the influence of this layer on the back contact behavior depending on its thickness and the sodium doping.^[19,20] To obtain a deeper insight into the CIGSe/back contact junction, it is essential to investigate the back contact behavior theoretically. In this regard, publications on numerical modeling of CIGSe solar cells with different back contacts exist.^[21,22] However, they have neglected the concurrent impact of back surface recombination velocity (S_b) and interface states on the solar cell parameters.

Similarly, defects are a crucial point in optimizing the performance of the CIGSe solar cells. Wei et al. calculated the possible defect types and their energetic depth.^[23] Nevertheless, defects applied in simulations were pure Shockley–Read–Hall recombination centers in midgap without investigating different distributions.^[4,5,8] Yet, a more detailed and realistic implementation of defects could benefit our understanding of the CIGSe solar cell performance.

Our work aims at developing a realistic model for CIGSe solar cells on Mo and ITO back contacts concerning, in particular, the influence of doping density, Schottky barrier, back surface interface states, and different defect densities and distributions. The parameters are adjusted to fit our experimental results. Moreover, the resulting trends for parameter changes are shown to enable fast adjustability for fitting other experimental configurations. First, the model structure and our modeling approach are shown. Then, the optical and electrical simulation setup is explained, showing the parameter set. It follows the explanation of the theoretical background for the two back contact materials and settings for the defect distributions. Then, the back contact behavior is confirmed without the influence of bulk defects. It follows the investigation of parameter variations in the full model, leading to a fit for the experimental current–voltage (J – V) curves on Mo and ITO back contact.

2. Modeling Approach

We established a 2D optoelectrical simulation model of a CIGSe solar cell in COMSOL Multiphysics, which we will cross-check later with experimental results for ultrathin absorbers. In the following, we present the layer stack corresponding to the realistic structure, the optical and electrical simulation setups, a list of parameters, and details on the Schottky contact and defect distributions.

2.1. Structure

Our lab's CIGSe solar cells with a PVD-fabricated absorber on Mo or ITO back contact inspired the geometry. Details on the fabrication process for specifically the ultrathin solar cells with ITO back contact can be found in ref. [24]. The process used for cells with Mo back contact is comparable. In **Figure 1**, a schematic of the

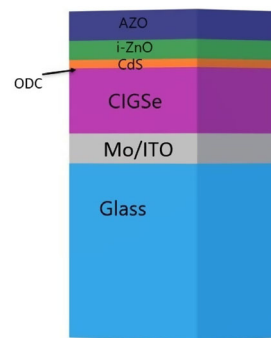


Figure 1. Layer stack consisting of 3 mm/700 μm glass, 800/300 nm Mo/ITO, 500 nm CIGSe including a 15 nm ODC layer, 50 nm CdS, 80 nm *i*-ZnO and 300 nm AZO.

simulated structure is shown. The structure starts with a 3 mm soda-lime glass substrate plus 800 nm Mo (with sodium diffusion barrier) or a 700 μm barium-borosilicate alkali-free glass substrate plus 300 nm ITO. A CIGSe absorber layer of 500 nm thickness, with an ordered defect compound layer (n-type ODC) of 15 nm thickness included at the absorber front interface, is placed on top. The ODC is inserted to better model the CIGSe/CdS interface and the present defects.^[4,8,25] On top of the ODC layer, the 50 nm-thick CdS buffer layer, followed by the intrinsic zinc oxide (*i*-ZnO) and the aluminum-doped zinc oxide (AZO) layers with 80 and 300 nm thickness, respectively, is added.

2.2. Optical Simulations

For the optical simulations, the wave optics module in COMSOL was applied to the 2D cell stack introduced above. Additionally, perfectly matched layers (PMLs) were added at the top and bottom, and periodic boundary conditions were applied for the side walls. The required complex refractive indices of the different layers were derived via a mathematical approach based on the transfer matrix method. For this purpose, transmission and reflection spectra of the individual layers were measured by UV–Vis spectrometry in the MultiOptix Group at the University of Duisburg-Essen or at the Helmholtz Zentrum Berlin.^[26] Then, the software RefDex^[27] was used to extract the refractive indices taking the thickness of the individual layers into account. Additionally, the roughness of each layer can be applied to refine the data.

The derived complex refractive indices were inserted into COMSOL to calculate the electric field distribution in the solar cell stack by solving the time-harmonic Maxwell equations with the finite element method.

From the field distribution, the CIGSe absorption and the total carrier generation rate were calculated in the simulation range from 350 to 1200 nm.^[28] The CIGSe absorption spectra on Mo and ITO can be found in the supplementary (Figure S1, Supporting Information). The generation rate implies the electron–hole pair generation in the solar cell due to photon absorption. For the simulations, the standard test conditions (STCs) were applied using the AM1.5G sunlight spectrum with 1000 W m^{–2} of input power density at a cell temperature of 25 °C to match the measurement conditions for the experimental results.

2.3. Electrical Simulations

For the electrical simulations, the semiconductor module in COMSOL was used. The before calculated generation rate for AZO, *i*-ZnO, CdS, and ODC/CIGSe was imported. Based on it, the module solves the drift and diffusion equations under illuminated conditions.

To develop our own parameter set, we started with published parameters and identified the most affecting ones. Then, we added defects and adjusted the parameters to fit our experimental data. Furthermore, we investigated the effects of parameter variations. The used parameters are summarized in **Table 1**. There are three categories of parameters: 1) Inherently fixed parameters such as bandgap (E_g), electron affinity (χ), and relative permittivity (ϵ_r) of layers are chosen according to the values in the literature.^[4,5,8,29,30] Moreover, the values for electron and hole mobility (μ_n, μ_p) were set to the numbers used in most publications. The ODC, being the boundary layer of CdS/CIGSe, shares the electron affinity and lifetime with CIGSe and the doping density with CdS. Due to the electron–hole pair generation in the CIGSe (the absorber layer) and the specified GGI (Ga/(Ga + In)) ratio in our experiment, the density of states (DOS) in the valence and conduction band (VB and CB) of CIGSe were calculated.^[31] Therefore, knowing the effective mass

of electrons and holes is essential. The effective electron and hole mass (m_e^*/m_h^*) in CIGSe can be tuned by the GGI (Ga/(Ga + In)) ratio.^[32] For our case of GGI = 0.31, $m_e^* = 0.1m^*$ and $m_h^* = 0.3m^*$ where m^* is the effective mass of a free electron. As two different back contact materials were used in the simulations, the neutrality energy level was considered constant at $0.2 E_g$ for Mo and $0.8 E_g$ for ITO. The energy level of traps (E_{def}) was fixed at $0.1 E_g$ for acceptor defects and $0.8 E_g$ for donor defects according to values calculated by Wei et al.^[23] 2) Several parameters did not show any significant effects on the simulation results; therefore, they were considered as fixed parameters and set to common literature values: doping densities, VB DOS, and CB DOS in the ODC, CdS, *i*-ZnO, and AZO, the lifetime of electrons and holes in all layers as well as electron and hole capture cross sections of traps in the CIGSe and ODC; and 3) In the third category of parameters are the ones of interest. These were identified as core parameters whose impact on the simulation results was investigated. The doping density (N_A) in CIGSe, as one variable parameter, was changed in the range of 10^{15} – 10^{16} cm⁻³, according to the ranges found in the literature.^[3,7,25,33] Additionally, defect densities (N_{def}) are of interest, which significantly impacted the cell performance. An acceptor defect density ($N_{def(A)}$), with a half Gaussian distribution from the back contact, was considered for the absorber in the range of 7×10^{10} to

Table 1. COMSOL simulation parameters of the standard CIGSe solar cell (VB DOS, density of states in the valence band; CB DOS, density of states in the conduction band; A, acceptor; D, donor; (Mo parameter/ITO parameter)).

Layer property	Symbol [unit]	Back contact	CIGSe	ODC	CdS	<i>i</i> -ZnO	AZO
Thickness	d [nm]	800/300	485	15	50	80	300
Bandgap	E_g [eV]		1.15 ^[4]	1.45 ^[25]	2.4 ^[30]	3.4 ^[30]	3.5 ^[29]
Electron affinity	χ [eV]		4.3 ^[3]	4.3	4.2 ^[29]	4.55 ^[25]	4.65 ^[29]
Relative permittivity	ϵ_r		13.6 ^[4,5,8,29,30]	13.6 ^[4]	10 ^[30]	9 ^[4,5,8,29,30]	9 ^[4,5,8,29,30]
VB DOS	N_v [cm ⁻³]		4.12×10^{18}	2×10^{18} ^[25]	1.5×10^{19} ^[30]	9×10^{18} ^[30]	9×10^{18} ^[30]
CB DOS	N_c [cm ⁻³]		7.96×10^{17}	2×10^{18} ^[25]	2×10^{18} ^[30]	4×10^{18} ^[30]	4×10^{18} ^[30]
Electron/hole mobility	μ_n, μ_p [cm ² V ⁻¹ s ⁻¹]		100, 25 ^[29]	1, 1 ^[25]	100, 25 ^[29]	100, 25 ^[29]	100, 25 ^[29]
Electron/hole lifetime	τ_n, τ_p [ns]		12, 1300 ^[29]	12, 1300	0.005, 0.005 ^[29]	0.005, 0.005 ^[29]	0.005, 0.005 ^[29]
Doping	N_A, N_D [cm ⁻³]		Variable (1×10^{15} / 1×10^{15}) (A)	5×10^{17} (D)	5×10^{17} (D) ^[5]	1×10^{18} (D) ^[25]	1×10^{20} (D) ^[5]
Density of defects	N_{def}		Variable (9×10^{11} / 2×10^{12}) (A) [cm ⁻²]	Variable (3×10^{18} / 2×10^{18}) (D) [cm ⁻³]	–	–	–
Energy level	E_{def} [eV]		$0.1 E_g$	$0.8 E_g$	–	–	–
Electron/hole capture cross sections	σ_w, σ_h [cm ²]		3×10^{-13} , 1×10^{-15} ^[5]	3×10^{-13} , 1×10^{-15} ^[5]	–	–	–
Work function	φ_m [eV]	Variable (4.9/4.9)	–	–	–	–	–
Decay length of acceptor back gradient	$d_{backgrading}$ [nm]	–	Variable (100/25)	–	–	–	–
Interface properties							
CIGSe/back contact							
Back electron/hole surface recombination velocity	S_{bn}, S_{bp} [cm s ⁻¹]			$8 \times 10^5, 4 \times 10^5$			
Interface state density	D_i [cm ⁻²]			Variable (7×10^{11}) (A)			
Charge neutrality level	φ_0 [eV]			$0.2 E_g$ (Mo), $0.8 E_g$ (ITO)			

$9 \times 10^{11} \text{ cm}^{-2}$. The distribution is modified by a decay length ($d_{\text{backgrading}}$) from 25 to 200 nm, determining how far the defects reach into the absorber. For the ODC, a uniformly applied donor defect density ($N_{\text{def(D)}}$) was considered. Typical density values for defects range from 10^{13} to 10^{18} cm^{-3} depending on the material.^[3–5,7] Furthermore, the acceptor-type interface state density (D_i) was varied from 10^{10} to 10^{14} cm^{-2} due to 10^{15} cm^{-2} being the maximum density of dangling bonds in Mo as a body-centered cubic crystal.^[34] In addition, the work function of the back contact (ϕ_m) ranged from 4.6 to 4.95 eV. The range stems from the work function range of Mo and ITO from 4.2 to 5.24 eV depending on treatment approaches (e.g., annealing, etching). Further details can be found in the supplementary (Table S1 and S2, Supporting Information). As the back surface recombination velocity (S_b) indicates the number of recombination centers at the semiconductor/back contact interface, S_b was varied from 10^4 to 10^7 cm s^{-1} . However, there is an interconnection between S_b and D_i as a consequence of the recombination current density. S_b as a variable was assumed to be the same for the back surface recombination velocities of electrons and holes (S_{bn} and S_{bp}). However, S_b was fixed to the calculated value after investigating its impact. Further information on the calculation of S_b can be found in the supplementary. Table 1 states the values at which they were finally fixed to fit our experimental results for Mo/ITO back contact.

2.4. Schottky Barrier

To elucidate the impact of the back contact barrier on the J - V characteristics of the CIGSe solar cell, Figure 2 illustrates the general model for the junction of CIGSe (p -type semiconductor) and metal/degenerate semiconductor (Mo/ITO) as the back contact by considering interface states at the semiconductor surface. Interface states are introduced due to dangling bonds caused by breaking the periodicity of the bulk crystal or by surface contamination.^[35]

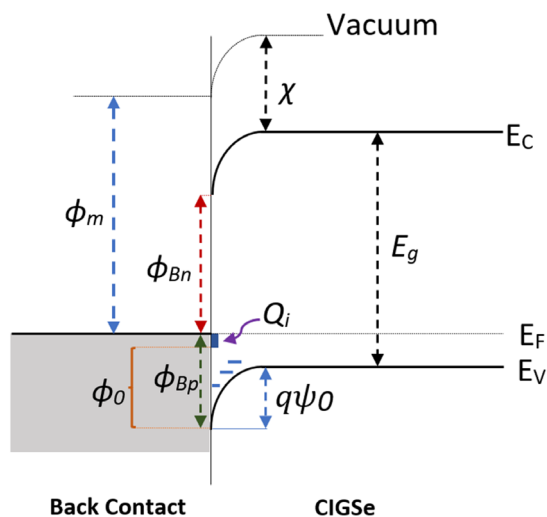


Figure 2. Schematic band diagram of the CIGSe/back contact interface with interface states.

As defined in Figure 2, the required material properties for assessing the Schottky barrier are: the bandgap energy of CIGSe E_g , its energy levels of conduction and valence bands E_C and E_V , respectively, and the electron affinity χ of CIGSe with respect to the vacuum level; the work function of the back contact (Mo or ITO), ϕ_m i.e., the energy required to transport an electron from the Fermi level E_F to the vacuum level; the charge neutrality level ϕ_0 below which the interface states are filled. ϕ_0 is measured from the edge of the valence band of the semiconductor. The surface charge density Q_i ($Q_i = qD_i(E_F - \phi_0)$ where q is the elemental charge), residing at the semiconductor interface, results from the interface state density D_i (cm^{-2}). Furthermore, the interfacial layer of thickness t has not been shown in Figure 2 because of its atomic scale.

By assuming the interface state density is independent of the metal properties and the atomic-scale thickness of the interfacial layer, the hole barrier height at the p -type CIGSe/back contact junction is^[36]

$$\phi_{Bp} = \gamma[E_g - (\phi_m - \chi)] + (1 - \gamma)\phi_0 \quad (1)$$

where γ is the interface state parameter, expressed as^[35]

$$\gamma = \frac{1}{1 + tD_i/K_i\epsilon_0} \quad (2)$$

where K_i is the dielectric constant of the interfacial layer.

According to Equation (1) and (2), special cases are of great interest. 1) $D_i \rightarrow \infty$, $\gamma = 0$ and then $\phi_{Bp} = \phi_0$; therefore, the Fermi level is pinned by the interface states at ϕ_0 . In this case, the model approaches the Bardeen limit where the barrier height is insensitive to the work function of the back contact; 2) $D_i = 0$, $\gamma = 1$ and then $\phi_{Bp} = E_g - (\phi_m - \chi)$ which leads to the ideal Schottky model.

The interface states create interface dipoles, which predominantly lead to a large electric field at the junction and a change in the band bending near the surface by shifting the Fermi level.^[37] Regarding the energetic position of the charge neutrality level, the additional electronic charge transfer can be directed from the back contact to the CIGSe layer or from CIGSe to the back contact, which affects the space-charge region (SCR) in CIGSe and consequently the band bending.^[38] The band bending describes the contact nature of “accumulation”, “neutral”, or “depletion”,^[35] as shown in Figure 3a–c. A good Ohmic contact requires obtaining the accumulation contact, which allows holes (majority carriers) to diffuse to the metal (Figure 3a). If the back potential ψ_0 is less than $k_B T/q$ (k_B is Boltzmann’s constant, and T is the temperature), the contact acts as quasi-Ohmic (see Figure 3b). In this case, holes can migrate to the metal but not as easily as for the Ohmic contact. When the Fermi energy of CIGSe is larger than the work function of the back contact before contact, ψ_0 arises, in which the holes in CIGSe should overcome to transit into the back contact (Figure 3c).

In order to decrease the interface state density, passivation may be desired. A large passivation area can be achieved by point-contact structures at the interface of the back contact and CIGSe.^[39,40] The passivation not only suppresses the number of interface states but also affects the charge distribution at the vicinity of the interface leading to a change in the back

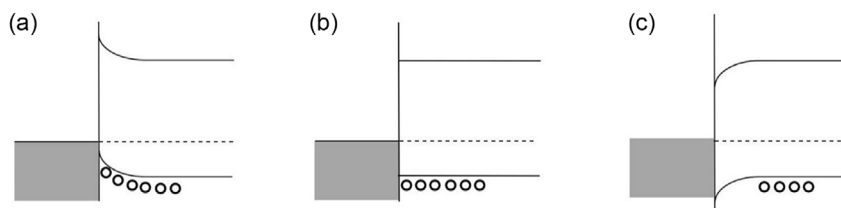


Figure 3. Band diagram of a CIGSe/back contact junction with different Fermi levels of CIGSe before contact due to the different interface state densities. a) “Accumulation” nature of the contact when φ_m is larger than the Fermi level of CIGSe. b) “Neutral” nature of the contact when φ_m is equal to the Fermi level of CIGSe. c) “Depletion” nature of the contact when φ_m is lower than the Fermi level of CIGSe.

surface recombination velocity.^[4,41] In other terms, passivation can reduce the number of the recombination centers, which are represented by the back surface recombination velocity. According to Tu et al. and Yong et al.,^[41,42] two distinct passivation behaviors have been observed for Mo and ITO: as passivation causes a decrease in surface recombination velocity, passivation of the back interface is beneficial for Mo while it would be detrimental for ITO due to the different contact nature.

2.5. Defects

To accurately model experimental results and understand what is the possible cause for certain behaviors, e.g., rollover, we applied different defect types and distributions to our model and observed their influence. Initial tests with the four different types available in COMSOL (acceptor, donor, neutral electron, and neutral hole traps) as homogeneously distributed defects and with different discrete energy levels showed that only acceptor and neutral electron traps take effect in *p*-type layers while the donor or neutral hole traps become active in *n*-type layers. A detailed explanation of the crystal defects and their respective trap types can be found in the supplementary (Table S3, Supporting Information).

Li et al.^[24] found experimentally that absorbers grown without sodium showed a rollover in the *J*–*V* characteristics, while absorbers grown with sodium postdeposition treatment (PDT) did not.^[24] Furthermore, the element depth profiles obtained by Li et al. revealed sodium aggregation at the back contact interface. The *J*–*V* data we use for fitting were obtained from samples produced with PDT. Due to the experimental findings, we chose to investigate a back-graded distribution of acceptor defects in the absorber bulk as shown in **Figure 4**. The acceptor defects will act as docking points for the sodium and will be passivated by sodium incorporation. For increasing sodium content, the acceptor defect density and depth distribution will be decreased.

The grading applied has a half-Gaussian shape with the decay length given by the width where the acceptor defect density is reduced to $1/e$ times its peak value. The shape resembles the sodium distribution shown by Li et al.^[24] A shallow acceptor trap was applied which can be linked to a Cu vacancy, a Se antisite, or a Se interstitial. These acceptor traps in COMSOL are negatively charged when unoccupied and are neutral when occupied. The sodium ions with positive charge will interact with the traps at the back contact neutralizing the charge. This yields the possibility to model the effect of sodium PDT with the acceptor defect density as well as the decay length applied to the distribution.

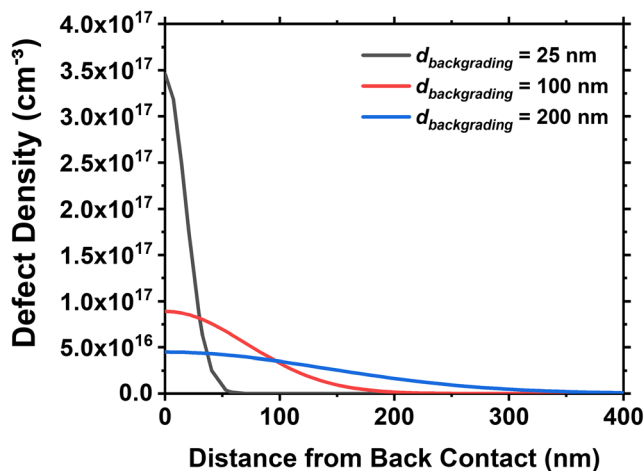


Figure 4. Example acceptor defect density distributions resulting from decay lengths of 25, 100, and 200 nm.

The earlier mentioned neutral electron traps cause the same effect; however, due to our hypothesis of sodium ions passivating the defects and the energetic positions close to the valence band, we chose the acceptor trap type. For determining the impact of $d_{\text{backgrading}}$, it is necessary to fix the surface charge density to keep the number of traps constant. To achieve this, we defined the acceptor trap density as surface density, which is divided by $d_{\text{backgrading}}$. Then, it yields the necessary volume density with a constant trap number for the COMSOL input.

For the ODC layer, we chose a homogenous defect distribution due to the small layer thickness. The deep donor traps applied can have multiple origins. One possible cause is a higher density of In_{Cu} and Ga_{Cu} antisites.^[23,43,44] Another reason may lay in Cd diffusion during the chemical bath deposition process, as shown by refs. [45,46]. Trap application in the buffer and window layer showed no effect on the simulation results and are omitted for this model.

For all defects, $E_{\text{def}}\text{s}$ are defined from the VB edge and their depths are based on the calculations of Zhang et al.,^[44] i.e., here the In_{Cu} antisites are at $0.8 E_g$ relative depth while the V_{Cu} are at $0.1 E_g$.

3. Results and Discussion

First, the impact of different back surface recombination velocities on the *J*–*V* characteristics is shown. Then, the impact of

interface states at the CIGSe/back contact on both hole barrier height and the PV parameters is demonstrated and discussed for the two different back contacts of Mo and ITO. After that, the combined influence of all varied parameters on the J - V characteristics is elaborated, showing how the fitting of open-circuit voltage (V_{oc}), short-circuit current density (J_{sc}), and shunt resistance (R_{sh}) can be adjusted.

3.1. Back Surface Recombination Velocity

Recombination current density ($j_{re} = S_b \times D_i$ (for interface) or $j_{re} = S_b \times N_{def}$ (for bulk)) is a factor influencing the overall current density of the solar cell.^[31,42] As S_b is one constituent of the recombination current density, examining the impact of S_b on the photovoltaic (PV) parameters is of great importance. **Figure 5** illustrates J_{sc} , V_{oc} , fill factor (FF), and efficiency (Eff) as a function of ϕ_{Bp} for S_b in the range from 10^4 to 10^7 cm s^{-1} . As it can be seen in Figure 5a, by an increase of ϕ_{Bp} in the range from 0 to 0.9, with 0.1 eV increment size, there is a general decrease of J_{sc} . The reason is a lower probability for holes to diffuse from CIGSe to the back contact with increasing hole barrier height, which effectively reduces the carrier collection at the back contact. In addition, increasing ϕ_{Bp} causes a decrease in ϕ_{Bn} (according to Figure 2, the electron barrier height ϕ_{Bn} is equal to $E_g - \phi_{Bp}$). Therefore, the probability of migrating electrons from the back contact to CIGSe increases for higher hole barriers. On the other hand, an increase in S_b implies that more charge carriers (electrons and holes) will recombine at the back interface of CIGSe before they can be collected and J_{sc} reduces. Therefore, with a higher back surface recombination velocity and

higher hole barrier, fewer electrons can be transported from the back contact over the barrier into CIGSe. However, the contribution of holes to the total current does not considerably change. Accordingly, J_{sc} increases because the total current density $j_t = |j_{hole}| + |j_{electron}|$ (j_{hole} : hole current density, $j_{electron}$: electron current density). Hence, there is a slight turning point at $\phi_{Bp} = 0.7$ eV.

Figure 5b illustrates that V_{oc} decreases as a function of ϕ_{Bp} for a given S_b ; however, the influence of increasing S_b affects V_{oc} negatively first (decreasing, blue arrow), and after that, it acts as a positive impact (increasing, red arrow). The transition between the trends is defined as a turning point (ϕ_T), which occurs at $\phi_{Bp} = 0.25$ eV. ϕ_T arises from the impact of S_b on the charge distribution and consequently V_{oc} . At ϕ_{Bp} lower than ϕ_T , higher recombination velocities diminish charge concentrations in the SCR. This reduction results from the higher hole recombination probability at the interface, which builds a separate SCR in the opposite polarity due to the hole depletion in the vicinity of the CIGSe/back contact interface. Accordingly, the effective electric potential in the main SCR gets lower, and hence V_{oc} . This trend continues up to the ϕ_T where the space charge density stays constant for all S_b s. However, for ϕ_{Bp} greater than ϕ_T , the negative impact of S_b on the SCR is suppressed,^[41] therefore, the increase in S_b results in higher electric potential because of the rise in charge concentrations which leads to higher V_{oc} . The increase in charge concentration is caused by two concurrent factors: 1) polarity change of SCR at the CIGSe/back contact interface into the constructive contribution; and 2) extension of this SCR further to the main SCR.

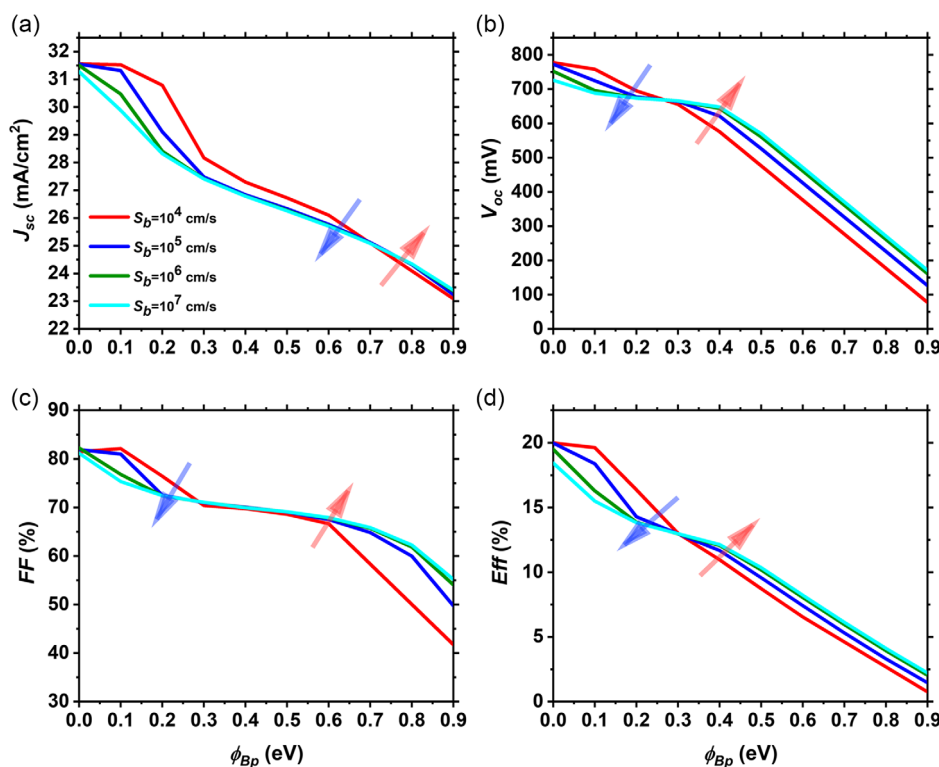


Figure 5. Photovoltaic parameters as a function of the hole barrier height ϕ_{Bp} and back surface recombination velocity S_b .

The dependency of FF and Eff on S_b and ϕ_{BP} is presented in Figure 5c,d, respectively. The dependency of FF on V_{oc} is the following^[47,48]

$$FF = \frac{V_{oc} - \ln(V_{oc} + 0.72)}{V_{oc} + 1} \quad (3)$$

where $V_{oc} = qV_{oc}/Ak_B T$ is the normalized voltage with A the ideality factor of the solar cell. Furthermore, Eff is a function of J_{sc} , V_{oc} , FF , and input power. Therefore, trends of FF (S_b , ϕ_{BP}) and Eff (S_b , ϕ_{BP}), which are similar to J_{sc} (S_b , ϕ_{BP}) and V_{oc} (S_b , ϕ_{BP}), can be observed. However, there is a slight shift in the turning point to a higher ϕ_{BP} of 0.3 eV. According to Equation (3), FF and hence Eff are nonlinearly dependent on V_{oc} and J_{sc} (affecting A), which can explain the observed shift.

Investigating the influence of surface recombination velocities is highly interesting against the background of experimental structures aiming at their manipulation. For the following generic simulations without additional interface structures, however, we set the values of S_{bn} and S_{bp} as given in Table 1. These values originate from the calculation via thermionic emission–diffusion theory as detailed in Equation (1) and (2) of the supplementary information.

3.2. Interface States

In this part, the influence of the interface state density, as another constituent of j_{re} , on the hole barrier height (Schottky barrier) and accordingly on the J – V characteristics is studied.

In order to investigate the correlation between the hole barrier height and the work function of the back contact, **Figure 6** demonstrates the ϕ_{BP} variations as a function of ϕ_m by considering different D_i at ϕ_0 s of $0.2 E_g$ and $0.8 E_g$, respectively. As it can be seen in Figure 6a, for $\phi_0 = 0.2 E_g$, the interface state parameter $\gamma = \frac{\partial \phi_{BP}}{\partial \phi_m}$ reduces with increasing D_i , and takes values of 1, 0.99, 0.99, 0.96, 0.23, and 0.05 for D_i equal to 0, 10^{10} , 10^{11} , 10^{12} , 10^{13} , and 10^{14} cm^{-2} , respectively. It reveals a decreasing dependency of ϕ_{BP} on ϕ_m with increasing D_i . Figure 6b represents the insignificant impact of D_i on the ϕ_{BP} – ϕ_m dependency at $\phi_0 = 0.8 E_g$. In this case, γ reduces from 1 to 0.98 only with D_i increasing from 0 to 10^{14} cm^{-2} . The D_i is rendered inactive. According to Equation (1), the hole barrier is highly dependent on the work function when γ is close to one. Consequently, this high sensitivity to the work function leads to the ideal Schottky-like contact (see Figure 3c).

To inspect the impact of the interaction of ϕ_0 and D_i on the nature of the CIGSe/back contact junction, the band diagrams of the CIGSe solar cell for the three different interface state densities 10^{10} , 10^{12} , and 10^{14} cm^{-2} are illustrated in **Figure 7**. Figure 7a shows that the different energy band levels consisting of E_C , E_V , E_{Fn} (electron quasi-Fermi level), and (E_{Fp}) (hole quasi-Fermi level) overlap each other at a low D_i of 10^{10} cm^{-2} for the two distinct charge neutrality levels of $0.2 E_g$ (solid lines) and $0.8 E_g$ (dashed lines), hence are indistinguishable in this plot. In this figure, ϕ_{BP} is 0.576 eV for both $\phi_0 = 0.2 E_g$ and $\phi_0 = 0.8 E_g$. As it can be seen in Figure 7b, increasing D_i to 10^{12} cm^{-2} lowers ϕ_{BP} to 0.477 eV for $\phi_0 = 0.2 E_g$ while it stays constant at 0.576 eV for $\phi_0 = 0.8 E_g$. In Figure 7c, ϕ_{BP} decreases

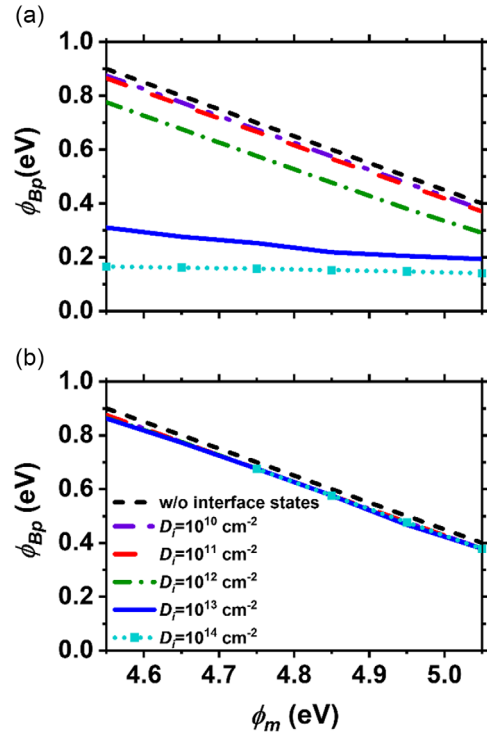


Figure 6. Calculated hole barrier heights as a function of the work function of the back contact by considering D_i from zero to 10^{14} cm^{-2} for a) $\phi_0 = 0.2 E_g$ and b) $\phi_0 = 0.8 E_g$.

to 0.15 eV for D_i of 10^{14} cm^{-2} and $\phi_0 = 0.2 E_g$ whereas the reduction in ϕ_{BP} is insignificant for $\phi_0 = 0.8 E_g$.

As shown in Figure 7c, for ϕ_0 of $0.2 E_g$, the quasi-Fermi level for holes aligns with the zero energy of the metal contact. Moreover, there is no band bending at the junction visible, the junction is neutral (see Figure 3b) and shows quasi-Ohmic behavior. However, the junction behavior is Schottky-like for ϕ_0 of $0.8 E_g$ because of ψ_0 . The established ψ_0 results from the depletion of holes in the vicinity of the back interface. The depletion region creates a downward band bending near the interface. Figure 7a–c confirm that the dependency of ϕ_{BP} on ϕ_m for higher D_i s at ϕ_0 of $0.2 E_g$ gets remarkably lower (Figure 6a) whereas ϕ_{BP} is still highly dependent on ϕ_m for ϕ_0 of $0.8 E_g$ (Figure 6b).

To study the impact of interface states on the J – V characteristics, **Figure 8** shows the dependence of J_{sc} and V_{oc} on the D_i and ϕ_0 for the ϕ_m of 4.9 eV. In Figure 8a, the 3.24 mA cm^{-2} rise in J_{sc} is caused by the increase of D_i from 10^{10} to 10^{14} cm^{-2} for a relative energy position of $\phi_0 = 0.2 E_g$. The increase in Q_i at the back interface, caused by an increase of D_i , leads to a lower hole potential barrier while increasing the electron barrier, which reduces the recombination and enhances the carrier collection. In addition, the increase in space charge density enhances V_{oc} considerably from 469 to 679 mV in the aforementioned D_i range for $\phi_0 = 0.2 E_g$, as shown in Figure 8b. By altering the relative energy position of interface states to $0.8 E_g$, the influence of D_i on J – V parameters has faded: J_{sc} increases only 0.1 mA cm^{-2} , V_{oc} by 11.4 mV. In this case, the variation in the Q_i at the back interface and the space charge density causing more efficient carrier collection and more electric potential, respectively, is not noticeable.

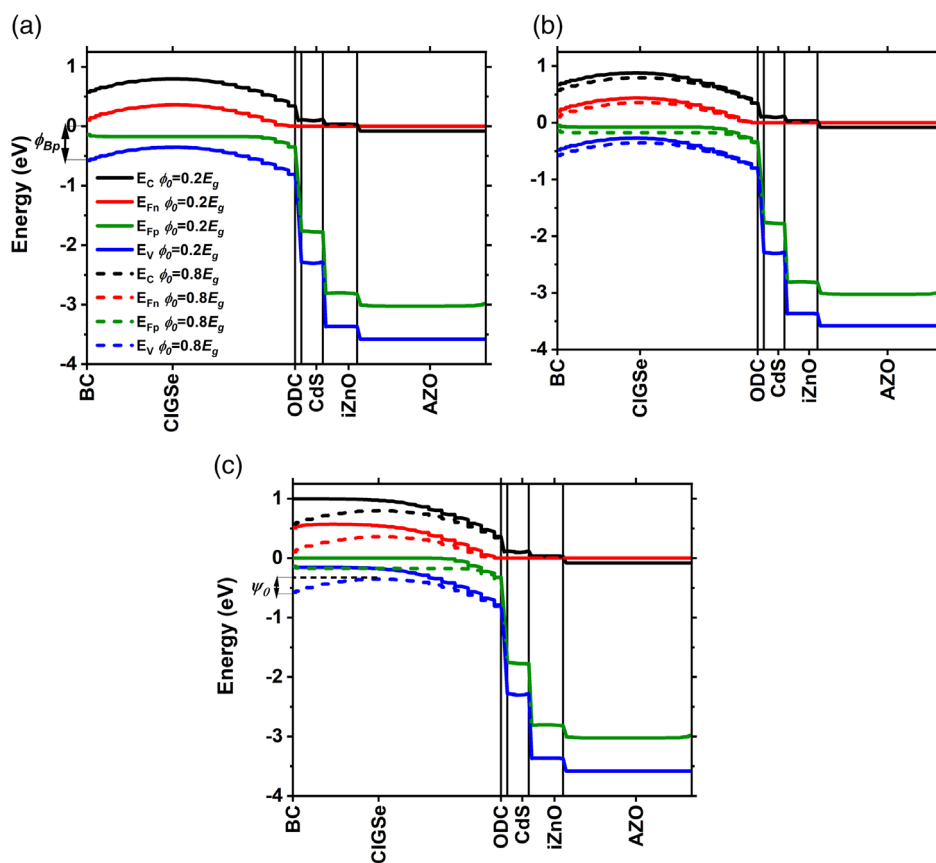


Figure 7. Energy band diagram of the CIGSe solar cell by considering the conduction band (E_C), the valence band (E_V), the electron quasi-Fermi level (E_{Fn}), and the hole quasi-Fermi level (E_{Fp}) for different concentrations of D_i : a) 10^{10} cm^{-2} , b) 10^{12} cm^{-2} , and c) 10^{14} cm^{-2} with two distinct ϕ_0 of $0.2 E_g$ (solid line) and $0.8 E_g$ (dashed line) (work function $\phi_m = 4.9 \text{ eV}$). (BC stands for back contact).

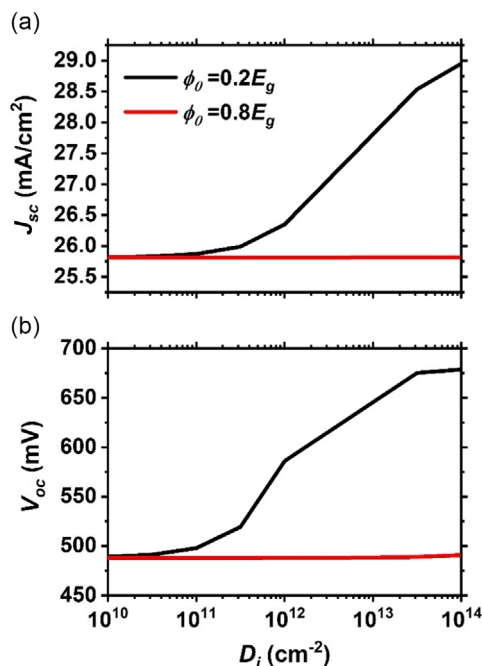


Figure 8. Variation of a) J_{sc} and b) V_{oc} as a function of D_i and ϕ_0 when the work function is 4.9 eV .

Therefore, the interface states can be described as inactive due to the neutral energy level of $0.8 E_g$.

These simulations demonstrate that it is possible to engineer the height of the barrier at the CIGSe/back contact interface and hence the behavior of the junction by considering the interface state density. All in all, regarding the 4.9 eV work function in our simulations, taken as the average of the work functions of Mo and ITO, the hole barrier height is 0.6 eV for both ITO and Mo back contact without any interface state density. On the other hand, the barrier height can be tuned by the interface states and their neutrality energy level which severely affect the behavior of the interface of CIGSe/back contact. In our case, the charge neutrality levels of $0.2 E_g$ and $0.8 E_g$ were considered to represent Mo and ITO, respectively. Regarding $\phi_0 = 0.2 E_g$ and D_i of 10^{14} cm^{-2} for Mo, the hole barrier height lowers to 0.15 eV ; accordingly, the behavior of the Mo/CIGSe interface can be found at the left hand of the turning point φ_T in Figure 5b. However, the barrier height for the ITO/CIGSe interface, where the charge neutrality level lies at $0.8 E_g$, remains constant for different interface state densities. Thus, the behavior of this interface is still at the right hand of φ_T . Therefore, the reduction in S_b (equal to reducing the interface recombination by passivation) results in better performance for the CIGSe solar cells with Mo back contact. Nevertheless, the trend is apparently opposite for the CIGSe solar cells on ITO.

3.3. Trends for J - V Parameter Adjustments

After the evaluation of S_b , D_i , φ_0 , φ_m , and φ_{BP} without the presence of other defects, we found that adding D_i and changing φ_m are not yet sufficient to fit the experimental J - V results. We further investigate the combined effects of D_i and φ_m with the additional parameters of doping density in the absorber (N_A), an acceptor defect gradient in the bulk ($N_{def(A)}$) with its decay length ($d_{backgrading}$), and the donor defect in the ODC ($N_{def(D)}$) on the J - V characteristics. The impact of these will be shown and discussed in the following for Mo. For ITO the parameters to fit the experimental results are fixed at different values, which will be stated for each part. Overall trends for Mo and ITO back contact stay the same.

3.3.1. Open-circuit Voltage

First, the impact on V_{oc} of D_i , φ_m , $N_{def(A)}$, and $d_{backgrading}$ is shown. The other mentioned parameters did not show a significant impact and were therefore set constant to the values given in Table 1.

In **Figure 9a**, the D_i sweep from 1×10^{10} to $7 \times 10^{11} \text{ cm}^{-2}$ is shown. Here, the other parameters are held constant at the values indicated by the green dashed lines in **Figure 9b-d**. Higher values as shown in the simulation without defects (**Figure 8**) stopped the simulation from converging due to a too large disturbance in charge carrier concentration. This sweep raises the open-circuit voltage from 600 mV to about 630 mV. The interface states will introduce additional charges at the back interface modifying the band diagram, as shown in **Figure 7a-c**. The negative

charges enlarge the back SCR and reduce the hole barrier, effectively rising the V_{oc} . For ITO, D_i is the same, however, the charge neutrality level changes to $0.8 E_g$.

Next, **Figure 9b** investigates a variation of φ_m between 4.6 and 4.95 eV to simulate the different back contact material properties and show their possible impact. The open-circuit voltage changes from 360 mV for a work function of 4.6 eV up to 650 mV for a work function of 4.95 eV. This large change is caused by the direct impact of the work function on the Schottky barrier. Higher work functions raise the electron barrier. Electrons are now easier repelled from the back contact, which increases the electric field that can build up. The choice of back contact material is crucial for the cell performance; however, minor differences in work function might be compensated by the interface states. The average work function of 4.9 eV proved our previous statement to be suitable for simulation of ITO and Mo back contact and therefore it is the value used for the parameter sweep and fit.

Additionally, **Figure 9c** reveals the sweep of $d_{backgrading}$ between 25 and 200 nm. The V_{oc} raises from 525 to 630 mV for the decay length between 25 and 100 nm, while the J - V curve starts to show a rollover for decay lengths higher than 100 nm (not shown here). The distribution of defects impacts the accumulation of negative charges at the back barrier. The back SCR is widened for $d_{backgrading}$ between 25 and 100 nm changing the band bending toward the back contact. Above 100 nm, the defects are reaching further into the SCR, which will affect the electric field distribution causing the rollover for higher applied bias voltage. For the ITO case, $d_{backgrading}$ is fixed at 25 nm for the other parameter variations. For the different contact materials, a different back gradient is expected.

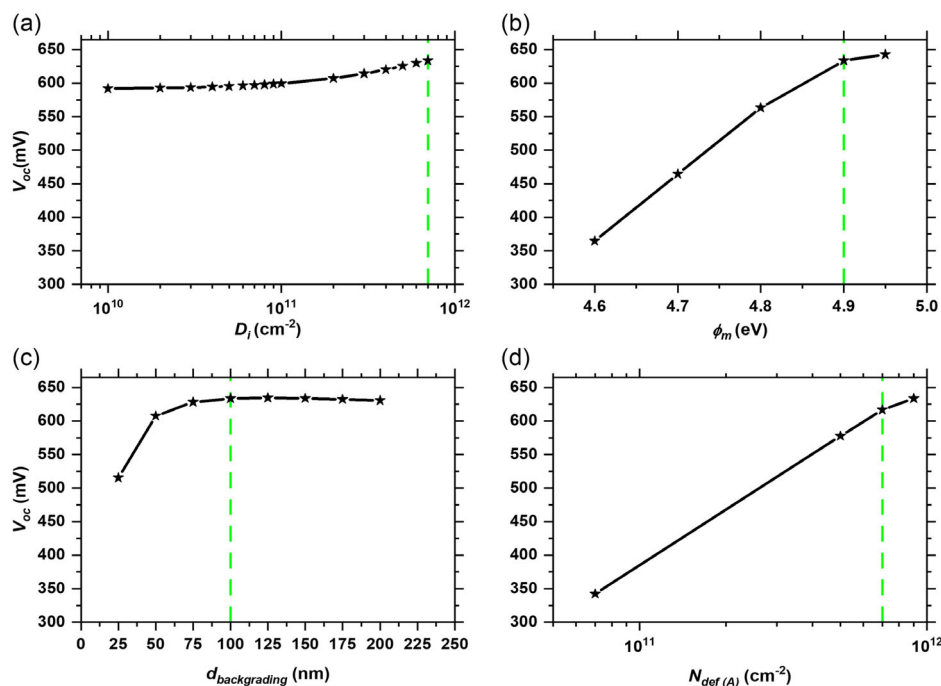


Figure 9. Open-circuit voltage V_{oc} change by variation of a) D_i , b) φ_m , c) $d_{backgrading}$, and d) $N_{def(A)}$. The green dashed lines indicate the values of the parameters when fixed in another sweep.

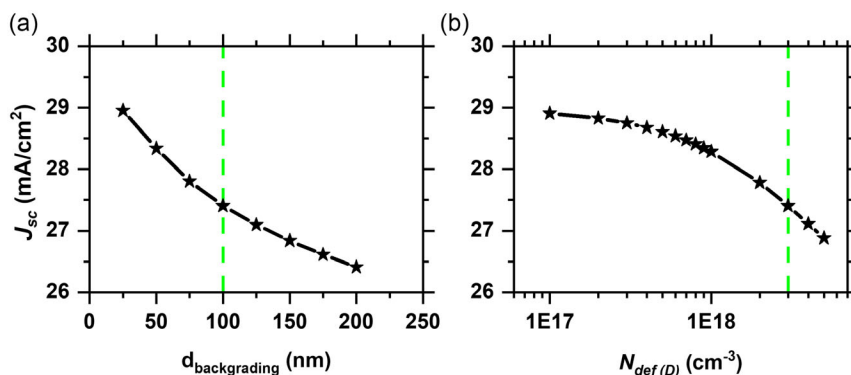


Figure 10. Short circuit current density change by varying a) $d_{backgrading}$ of the acceptor defects and b) $N_{def(D)}$ in the ODC layer. The green dashed lines indicate the values of the parameters when fixed in another sweep.

Finally, Figure 9d shows the impact of $N_{def(A)}$ swept between 7×10^{10} and 9×10^{11} cm⁻² while keeping the decay length constant to change the number of defects in the volume. The increase in total number of defects causes a rise in negative charge density; therefore, the back barrier for electrons is increased influencing the V_{oc} , which changes from 330 to 630 mV. In case of the ITO back contact, an acceptor defect density of 2×10^{12} cm⁻² is used as fixed value for the other parameter variations. This is higher than the actual range applied for Mo, which ended at 9×10^{11} cm⁻². For ITO, the charge neutrality level for the interface states changes to $0.8 E_g$ and makes a larger density possible.

3.3.2. Short-circuit Current Density

The J_{sc} is only significantly influenced by two of the varied parameters, and the other parameters show only minor effects. In Figure 10, the effects on the J_{sc} of $d_{backgrading}$ of the acceptor defects and $N_{def(D)}$ in the ODC are shown. (The acceptor defect density itself has no effect only the distribution parameter $d_{backgrading}$).

Figure 10a highlights the impact of a $d_{backgrading}$ sweep from 25 to 200 nm. The J_{sc} drops from 29 to 26.5 mA cm⁻². The reason is the defects reaching further into the SCR with longer decay length, thus increasing the number of recombination

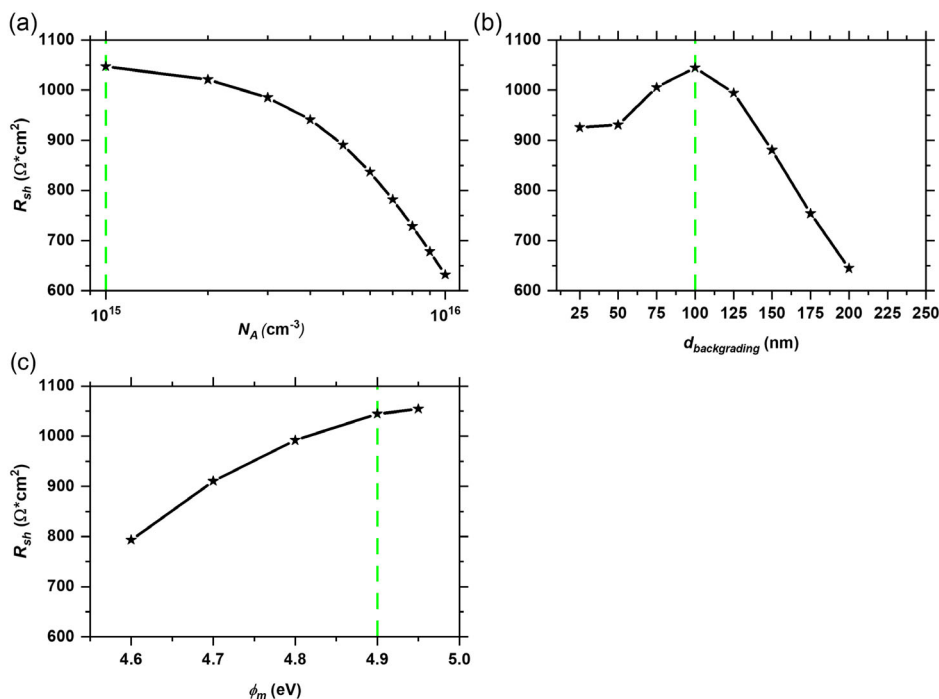


Figure 11. Shunt resistance R_{sh} change by varying a) N_A , b) $d_{backgrading}$, and c) ϕ_m . The green dashed lines indicate the values of the parameters when fixed in another sweep.

centers for the newly generated electron–hole pairs. The electron–hole pairs will recombine directly in the SCR consequently reducing J_{sc} .

Next, Figure 10b shows the $N_{def(D)}$ sweep from 9×10^{16} to $5 \times 10^{18} \text{ cm}^{-3}$. The J_{sc} drops from 29 to 26.8 mA cm^{-2} . The ODC layer is right at the front interface of the absorber and builds the p – n junction with the absorber bulk. The position of defects in direct vicinity of the p – n junction causes the generated charge carriers to directly recombine and reduce the collected current, without influencing any other J – V properties. $N_{def(D)}$ for the ITO back contact is fixed to $2 \times 10^{18} \text{ cm}^{-3}$ for the other parameter variations; the reason is a generally higher J_{sc} observed in the experimental results for ITO back contact.

3.3.3. Shunt Resistance

In Figure 11, the effects of parameter variations on the shunt resistance are shown. From the previously discussed parameters, only $d_{backgrading}$ and φ_m have influence on the shunt resistance. Additionally, N_A affects the shunt resistance without influencing J_{sc} or V_{oc} .

In Figure 11a, N_A has been varied from 10^{15} to 10^{16} cm^{-3} and the shunt resistance drops from 1050 to $620 \Omega \text{ cm}^2$ for higher doping densities. The lower doping of the CIGSe layer enlarges the space charge region inside the absorber and enhances the charge separation.

The variation of the decay length from 25 to 100 nm raises the shunt resistance from 920 to $1050 \Omega \text{ cm}^2$, as illustrated in Figure 11b. After the peak at 100 nm, R_{sh} drops to $625 \Omega \text{ cm}^2$ at 200 nm. The defects alter the charge distribution inside the absorber. For the decay lengths up to 100 nm, the position of the charges enhances the electric field, while for decay lengths larger than 100 nm recombination centers are introduced inside the SCR. These will directly influence the resistance; the possibility of recombination in these centers will increase with the number of passing charge carriers and the electric field breaks down easier. In Figure 11c, the work function of the back contact has been varied from 4.6 to 4.95 eV and an increase in shunt

resistance from 800 to $1050 \Omega \text{ cm}^2$ observed. For higher work functions, the electron barrier will increase causing the electrons to be more effectively repelled.

Given the trends shown in the previous section compared to our experimental results, we chose $D_i = 7 \times 10^{11} \text{ cm}^{-2}$, $\varphi_m = 4.9 \text{ eV}$, $d_{backgrading} = 100 \text{ nm}$, $N_{def(A)} = 9 \times 10^{11} \text{ cm}^{-2}$, $N_A = 1 \times 10^{15} \text{ cm}^{-3}$ for the Mo contact and $D_i = 7 \times 10^{11} \text{ cm}^{-2}$, $\varphi_m = 4.9 \text{ eV}$, $d_{backgrading} = 25 \text{ nm}$, $N_{def(A)} = 2 \times 10^{12} \text{ cm}^{-2}$, $N_A = 1 \times 10^{15} \text{ cm}^{-3}$ for the ITO contact. These values have been presented in Table 1 as the final parameter values applied in our simulations. While investigating the effect of the varied parameters on the J – V characteristics, we have observed no significant effect on series resistance R_s and FF by any of the varied parameters. Therefore, no evaluation of effects on R_s and FF will be shown.

3.4. Effects of Back Grading on the Band Diagram

Given the impact of the decay length on V_{oc} , J_{sc} , and R_{sh} , we look at the changes in band diagram between the two extrema 25 (solid line) and 200 (dashed line) nm decay length. The band diagrams are shown in Figure 12.

E_C and E_V show a similar behavior to the E_{Fn} with a higher and steeper bending for 200 nm (dashed lines) reaching further into the absorber bulk. For the E_{Fp} and 200 nm decay length, the curve does not follow the trend of the other dashed lines and stays constant over 300 nm and then drops steeper as the 25 nm decay length line. Due to the sharp bending for 200 nm, the hole barrier is larger. This increase in hole barrier makes it harder for the holes to reach the back contact, which increases the probability of recombination, due to reaching their lifetime, which affects the J_{sc} . Moreover, the V_{oc} is affected by raised barrier height in the E_C , increasing the built-in potential. However, the steeper slope toward the ODC for 200 nm reaches far into the SCR, close to the ODC, causing the rollover behavior.

3.5. Challenges in Fitting

One goal has been to understand our experimental results better and to be able to model cells on Mo and ITO back contact confidently. In Figure 13, the experimentally recorded J – V data obtained from the best cells of representative baseline samples for each back contact material, plotted as circles, are compared to the simulation data shown with dashed lines and a simulation data corrected by R_s (solid lines). The parameter set summarized in Table 1 is the optimized list for fitting our experimental curves resulting from the discussed parameter changes in the previous sections.

For the molybdenum back contact (red), the experimental result shows a J_{sc} of 27.30 mA cm^{-2} and the simulation result (without addition of R_s) differs by only 0.03 mA cm^{-2} . In the experiment V_{oc} is 634.00 mV , the difference to simulation 0.25 mV . A larger difference can be found for FF , which is 71.49% in experiment and 80.10% in simulation. Furthermore, the R_{sh} can be matched with the experimental data. The R_s cannot be matched by parameter variation and all results show a lack of R_s . This R_s deficit can be adjusted by adding an additional contact resistance in the COMSOL program. For the

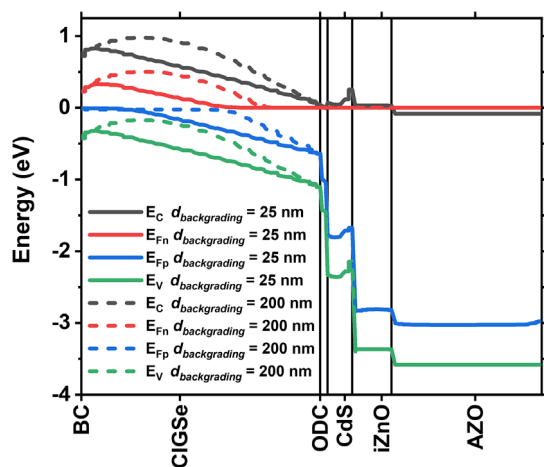


Figure 12. Impact of defect density distribution on the band diagram, shown for $d_{backgrading}$ of 25 and 200 nm. Here BC stands for back contact.

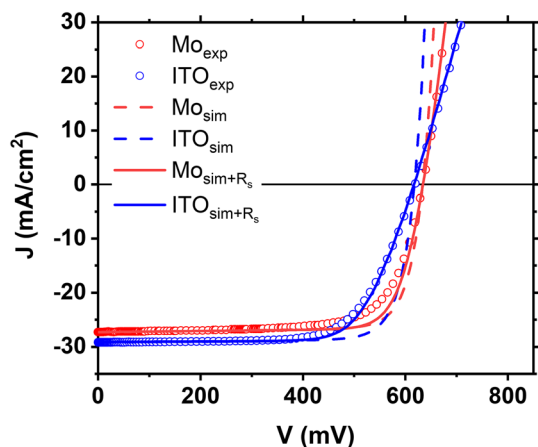


Figure 13. Comparison of experimental J - V curves for the best cells from representative baseline samples for ITO and Mo back contact with the simulated counterparts.

Mo simulation, $0.8 \Omega R_s$ was added, which matches the experimental R_s and reduces the simulated FF to 76.94%.

In case of ITO back contact (blue), the differences in simulation and experiment are similar. J_{sc} is 29.19 and 29.11 mA cm^{-2} for experimental and simulation data, respectively. The V_{oc} for the experiment has been measured at 618.99 mV while the simulation shows 616.16 mV. Additionally, the FF is measured with 67.96% for the experiment and reaches 80.48% in the simulation. Moreover, the R_{sh} matches between simulation and experiment. For ITO, R_s has been adjusted to 2.4Ω , which reduces the FF to 71.19%. A close match with the experimental curve has been achieved. Nevertheless, the FF remains unmatched for both back contact types.

4. Conclusion

Our aim was to develop a realistic model capable of simulating CIGSe solar cells with Mo and ITO back contact. We detail the influence on the J - V characteristics of the work function of the back contact (φ_m), the interface states at the back contact (D_i), the charge neutrality level of D_i (φ_0), the acceptor defect density ($N_{def(A)}$) in a Gaussian gradient distribution defined by the decay length ($d_{backgrading}$), and the donor defects ($N_{def(D)}$) in the ODC layer at the p - n interface as well as the doping density in the absorber layer N_A . All shown trends enable a fast adjustability of simulations to fit experimental results.

Our model can fit the J - V characteristics of CIGSe solar cells with Mo and ITO back contact by changing φ_0 of D_i , adjusting $N_{def(A)}$ and $d_{backgrading}$ at the back interface and $N_{def(D)}$ in the ODC. For Mo, the interface states reduced the barrier; hence, the interface at CIGSe/Mo acts as a quasi-Ohmic contact. It is a good description for the presence of MoSe_2 at the junction of Mo and CIGSe. Regardless of the density of interface states at the CIGSe/ITO interface, the higher φ_0 causes only a slight change in the barrier height for holes; consequently, the Schottky-like contact persists at the interface of ITO and CIGSe. There is still an open question about which parameters

experimentally influence the fixed Schottky-like contact or how it can be altered. The possibilities can lay in the thickness of GaO_x as an interlayer to CIGSe, the sputtering condition of ITO, the temperature of CIGSe deposition, or diffusion of other dopants into the interfacial layer.

The dependency of V_{oc} on D_i , $N_{def(A)}$ and $d_{backgrading}$ as well as φ_m was shown. D_i influences the V_{oc} less profoundly, while φ_m and $N_{def(A)}$ have significant impact. The decay length increases V_{oc} for $d_{backgrading}$ up to 100 nm, and then it saturates. By fixing φ_m according to the back contact material, and adjusting the defects and the grading parameter to adjust the V_{oc} , the ITO and Mo experimental results can be matched. The V_{oc} as a function of φ_{Bp} and S_b has a decisive role in characterizing the behavior of the CIGSe/back contact. We show that for barrier heights lower than 0.25 eV, V_{oc} decreases with the increase of surface recombination velocity whereas the declining trend converts to a rising one for barriers higher than this value. This pivotal role stems from the change in charge distribution depending on the surface recombination velocity.

The different defect distributions also showed an influence on J_{sc} . Especially $N_{def(D)}$ close to the p - n junction shows a major impact. Additionally, by rising $d_{backgrading}$, J_{sc} reduces while also influencing V_{oc} and R_{sh} . An increase in the hole barrier height causes a lower J_{sc} due to the lower density of holes diffusing to the back contact. Furthermore, the surface recombination velocity as a constituent for illustrating the number of recombination centers in CIGSe has a detrimental impact on J_{sc} . Additionally, $N_{def(D)}$ close to the CdS interface inside the ODC has a similar influence on J_{sc} like the decay length, without affecting other characteristics. The effect for the ODC defects is mainly due to the additional recombination centers close to the p - n junction, which can annihilate the newly generated charge carriers.

N_A , $d_{backgrading}$, and φ_m show impact on R_{sh} . With higher doping of the CIGSe layer, the shunt resistance reduces, while for larger work functions it is increased. The decay length can also be used to boost or reduce R_{sh} . Adjustments on the series resistance and hence the FF can only be achieved via an additional contact resistance in the simulation.

A final comparison of experimental and simulation results confirms that the used parameters are a good baseline for modeling ultrathin CIGSe solar cells. Moreover, being established in 2D, the model can act as the baseline parameter set for more advanced 2D and 3D simulations of different absorber thicknesses and geometries including microabsorbers, nanostructures, or point contacts.

Acknowledgements

J.L. and S.S. contributed equally to this work. J.L. and M.S. acknowledge the BMWK for funding via the KostSol project (FKZ: 03EE1029D). The authors thank Yong Li for providing his experimental data and the fruitful discussions.

Open Access funding enabled and organized by Projekt DEAL.

Conflict of Interest

The authors declare no conflict of interest.

Data Availability Statement

The data that support the findings of this study are available from the corresponding author upon reasonable request.

Keywords

chalcopyrite solar cells, defects, ITO back contacts, Mo back contacts, multidimensional modeling, optoelectrical modeling

Received: September 24, 2022

Revised: November 2, 2022

Published online:

- [1] A. M. Bradshaw, B. Reuter, T. Hamacher, *Green* **2013**, 3, 93.
- [2] L. M. Mansfield, A. Kanevce, S. P. Harvey, K. Bowers, C. Beall, S. Glynn, I. L. Repins, *Prog. Photovolt. Res. Appl.* **2018**, 26, 949.
- [3] M. Burgelman, K. Decock, S. Khelifi, A. Abass, *Thin Solid Films* **2013**, 535, 296.
- [4] R. Kotipalli, O. Poncelet, G. Lia, Y. Zeng, L.A. Francis, B. Vermang, D. Flandre, *Sol. Energy* **2017**, 157, 603.
- [5] N. Rezaei, P. Procel, M. Simor, Z. Vroon, M. Zeman, O. Isabella, *Prog. Photovolt. Res. Appl.* **2020**, 28, 899.
- [6] D. Sancho-Martínez, M. Schmid, *J. Phys. D Appl. Phys.* **2017**, 50, 445501.
- [7] A. Khadir, *Acta Phys. Pol. A* **2020**, 137, 11282020.
- [8] J. Lontchi, M. Zhukova, M. Kovacic, J. Krc, W. C. Chen, M. Edoff, S. Bose, P. M. Salomé, J. Goffard, A. Cattoni, L. Gouillart, *IEEE J. Photovolt.* **2020**, 10, 1908.
- [9] A. F. Violas, A. J. Oliveira, J. P. Teixeira, T. S. Lopes, J. R. Barbosa, P. A. Fernandes, P. M. Salomé, *Sol. Energy Mater. Sol. Cells* **2022**, 243, 111792.
- [10] D. Abou-Ras, A. Nikolaeva, S. Caicedo Dávila, M. Krause, H. Guthrey, M. Al-Jassim, M. Morawski, R. Scheer, *Sol. RRL* **2019**, 3, 1900095.
- [11] K.-J. Hsiao, J.-D. Liu, H.-H. Hsieh, T.-S. Jiang, *Phys. Chem. Chem. Phys.* **2013**, 15, 18174.
- [12] N. Neugebohrn, M. S. Hammer, J. Neerken, J. Parisi, I. Riedel, *Thin Solid Films* **2015**, 582, 332.
- [13] N. Nicoara, R. Manaligod, P. Jackson, D. Hariskos, W. Witte, G. Sozzi, R. Menozzi, S. Sadewasser, *Nat. Commun.* **2019**, 10, 3980.
- [14] P. J. Rostan, J. Mattheis, G. Bilger, U. Rau, J. H. Werner, *Thin Solid Films* **2005**, 480–481, 67.
- [15] X. Zhang, M. Kobayashi, A. Yamada, *ACS Appl. Mater. Interfaces* **2017**, 9, 16215.
- [16] A. Mavlonov, T. Nishimura, J. Chantana, Y. Kawano, T. Masuda, T. Minemoto, *Sol. Energy* **2020**, 211, 1311.
- [17] F. Mollica, M. Jubault, F. Donsanti, A. Loubat, M. Bouttemy, A. Etcheberry, N. Naghavi, *Thin Solid Films* **2017**, 633, 202.
- [18] J.-H. Yoon, J. H. Kim, W. M. Kim, J. K. Park, Y. J. Baik, T. Y. Seong, J. H. Jeong, *Prog. Photovolt. Res. Appl.* **2014**, 22, 90.
- [19] M. Saifullah, D. Kim, J. S. Cho, S. Ahn, S. Ahn, J. H. Yun, H. S. Lee, J. H. Park, *J. Mater. Chem. A* **2019**, 7, 21843.
- [20] Y.-S. Son, H. Yu, J. K. Park, W. M. Kim, S. Y. Ahn, W. Choi, D. Kim, J. H. Jeong, *J. Phys. Chem. C* **2019**, 123, 1635.
- [21] B. Barman, P. K. Kalita, *Sol. Energy* **2021**, 216, 329.
- [22] S. Yang, S. Khelifi, J. d. Wild, B. Vermang, J. Lauwaert, *Sol. Energy* **2021**, 228, 464.
- [23] S.-H. Wei, S. B. Zhang, A. Zunger, *J. Appl. Phys.* **1999**, 85, 7214.
- [24] Y. Li, G. Yin, Y. Gao, T. Köhler, J. Lucaßen, M. Schmid, *Sol. Energy Mater. Sol. Cells* **2021**, 223, 110969.
- [25] A. Niemegeers, M. Burgelman, R. Herberholz, U. Rau, D. Hariskos, H. W. Schock, *Prog. Photovolt. Res. Appl.* **1998**, 6, 407.
- [26] G. Yin, C. Merschjann, M. Schmid, *J. Appl. Phys.* **2013**, 113, 213510.
- [27] P. Manley, G. Yin, M. Schmid, <https://www.uni-due.de/ag-schmid/refdex.php> (accessed: June 2013).
- [28] W. Raja, M. Schmid, A. Toma, H. Wang, A. Alabastri, R. Proietti Zaccaria, *ACS Photonics* **2017**, 4, 2025.
- [29] F. Mollica, *Ph.D. Thesis*, Université Pierre et Marie Curie Paris, **2016**.
- [30] D. Sancho-Martínez, *Ph.D. Thesis*, FU Berlin **2018**.
- [31] S. M. Sze, K. N. Kwok, in *Physics of Semiconductor Devices*, John Wiley & Sons, Hoboken, NJ **2007**.
- [32] C. Persson, *Appl. Phys. Lett.* **2008**, 93, 072106.
- [33] T. N. Fridolin, D. K. G. Maurel, G. W. Ejuh, T. T. Bénédicte, N. J. Marie, *J. King Saud Univ. Sci.* **2019**, 31, 1404.
- [34] R. G. Ross, W. Hume-Rothery, *J. Less Common Met.* **1963**, 5, 258.
- [35] D. K. Schroder, D. L. Meier, *IEEE Trans. Electron Devices* **1984**, 31, 637.
- [36] C. R. Crowell, S. M. Sze, *Solid State Electron.* **1966**, 9, 1035.
- [37] L. Jelver, O. Hansen, K. W. Jacobsen, *Phys. Rev. B* **2021**, 104, 045313.
- [38] J. A. Spies, R. Schafer, J. F. Wager, P. Hersh, H. A. S. Platt, D. A. Keszler, G. Schneider, R. Kykyneshi, J. Tate, X. Liu, A. D. Compaan, *Sol. Energy Mater. Sol. Cells* **2009**, 93, 1296.
- [39] S. Bose, J. M. Cunha, S. Suresh, J. De Wild, T. S. Lopes, J. R. Barbosa, R. Silva, J. Borme, P. A. Fernandes, B. Vermang, P. M. Salomé, *Sol. RRL* **2018**, 2, 1800212.
- [40] G. Yin, M. Song, S. Duan, P. Manley, D. Greiner, C. A. Kaufmann, M. Schmid, *ACS Appl. Mater. Interfaces* **2016**, 8, 31646.
- [41] Y. Tu, Y. Li, R. Klenk, G. Yin, M. Schmid, *Prog. Photovolt. Res. Appl.* **2022**, 30, 393.
- [42] Y. Li, G. Yin, Y. Tu, S. Sedaghat, Y. Gao, M. Schmid, *ACS Appl. Energy Mater.* **2022**, 5, 7956.
- [43] S. Siebentritt, M. Igalson, C. Persson, S. Lany, *Prog. Photovolt. Res. Appl.* **2010**, 18, 390.
- [44] S. B. Zhang, S.-H. Wei, A. Zunger, H. Katayama-Yoshida, *Phys. Rev. B* **1998**, 57, 9642.
- [45] J. Kiss, T. Gruhn, G. Roma, C. Felser, *J. Phys. Chem. C* **2013**, 117, 25933.
- [46] T. Nakada, A. Kunioka, *Appl. Phys. Lett.* **1999**, 74, 2444.
- [47] D. L. Pulfrey, *Solid State Electron.* **1978**, 21, 519.
- [48] P. M. P. Salomé, A. Hultqvist, V. Fjällström, M. Edoff, B. G. Aitken, K. Zhang, K. Fuller, C. K. Williams, *IEEE J. Photovolt.* **2014**, 4, 1659.